Bioactive Materials 16 (2022) 271–284

Contents lists available at ScienceDirect

Bioactive Materials

journal homepage: www.keaipublishing.com/en/journals/bioactive-materials

Stratified-structural hydrogel incorporated with magnesium-ion-modified black phosphorus nanosheets for promoting neuro-vascularized bone regeneration

Yan Xu [a,1], Chao Xu [b,1], Lei He [a], Junjie Zhou [c], Tianwu Chen [d], Liu Ouyang [a], Xiaodong Guo [a], Yanzhen Qu [a,***], Zhiqiang Luo [b,**], Deyu Duan [a,*]

[a] Department of Orthopaedics, Union Hospital, Tongji Medical College, Huazhong University of Science and Technology, Wuhan, 430074, China
[b] College of Life Science and Technology, Huazhong University of Science and Technology, China Wuhan, 430022, China
[c] Department of Pathology, Union Hospital, Tongji Medical College, Huazhong University of Science and Technology, Wuhan, 430022, China
[d] Fudan University Sports Medicine Institute, Shanghai, 200040, China

ARTICLE INFO

Keywords:
Angiogenesis
Neurogenesis
Bone regeneration
Hydrogel
Black phosphorus

ABSTRACT

Angiogenesis and neurogenesis play irreplaceable roles in bone repair. Although biomaterial implantation that mimics native skeletal tissue is extensively studied, the nerve-vascular network reconstruction is neglected in the design of biomaterials. Our goal here is to establish a periosteum-simulating bilayer hydrogel and explore the efficiency of bone repair via enhancement of angiogenesis and neurogenesis. In this contribution, we designed a bilayer hydrogel platform incorporated with magnesium-ion-modified black phosphorus (BP) nanosheets for promoting neuro-vascularized bone regeneration. Specifically, we incorporated magnesium-ion-modified black phosphorus (BP@Mg) nanosheets into gelatin methacryloyl (GelMA) hydrogel to prepare the upper hydrogel, whereas the bottom hydrogel was designed as a double-network hydrogel system, consisting of two interpenetrating polymer networks composed of GelMA, PEGDA, and β-TCP nanocrystals. The magnesium ion modification process was developed to enhance BP nanosheet stability and provide a sustained release platform for bioactive ions. Our results demonstrated that the upper layer of hydrogel provided a bionic periosteal structure, which significantly facilitated angiogenesis via induction of endothelial cell migration and presented multiple advantages for the upregulation of nerve-related protein expression in neural stem cells (NSCs). Moreover, the bottom layer of the hydrogel significantly promoted bone marrow mesenchymal stem cells (BMSCs) activity and osteogenic differentiation. We next employed the bilayer hydrogel structure to correct rat skull defects. Based on our radiological and histological examinations, the bilayer hydrogel scaffolds markedly enhanced early vascularization and neurogenesis, which prompted eventual bone regeneration and remodeling. Our current strategy paves way for designing nerve-vascular network biomaterials for bone regeneration.

1. Introduction

Although bone tissue engineering made significant progress, correction of bone defects, caused by trauma and various bone diseases, remains a substantial challenge for surgeons [1]. Autografts are a golden standard for correcting bone defects. It promotes the design of artificial bone that mimics the structure and components of natural bone, such as, the nano-structure of calcium phosphate, addition of growth factors, local microenvironment, and so on. However, the results were unsatisfactory. This may be because the periosteum, particularly the neurovascular network that exists in periosteum, is often overlooked. It is well known that the vascular network in periosteum provides essential nutrients and growth factors for local osteogenesis. Meanwhile, the nerve in periosteum also activates and regulates the process of osteogenesis.

Peer review under responsibility of KeAi Communications Co., Ltd.
* Corresponding author.
** Corresponding author.
*** Corresponding author.
E-mail addresses: quyanzhen@hust.edu.cn (Y. Qu), zhiqiangluo@hust.edu.cn (Z. Luo), duandeyu@hust.edu.cn (D. Duan).
[1] Contributed equally to this work.

https://doi.org/10.1016/j.bioactmat.2022.02.024
Received 2 November 2021; Received in revised form 15 February 2022; Accepted 17 February 2022
Available online 28 February 2022

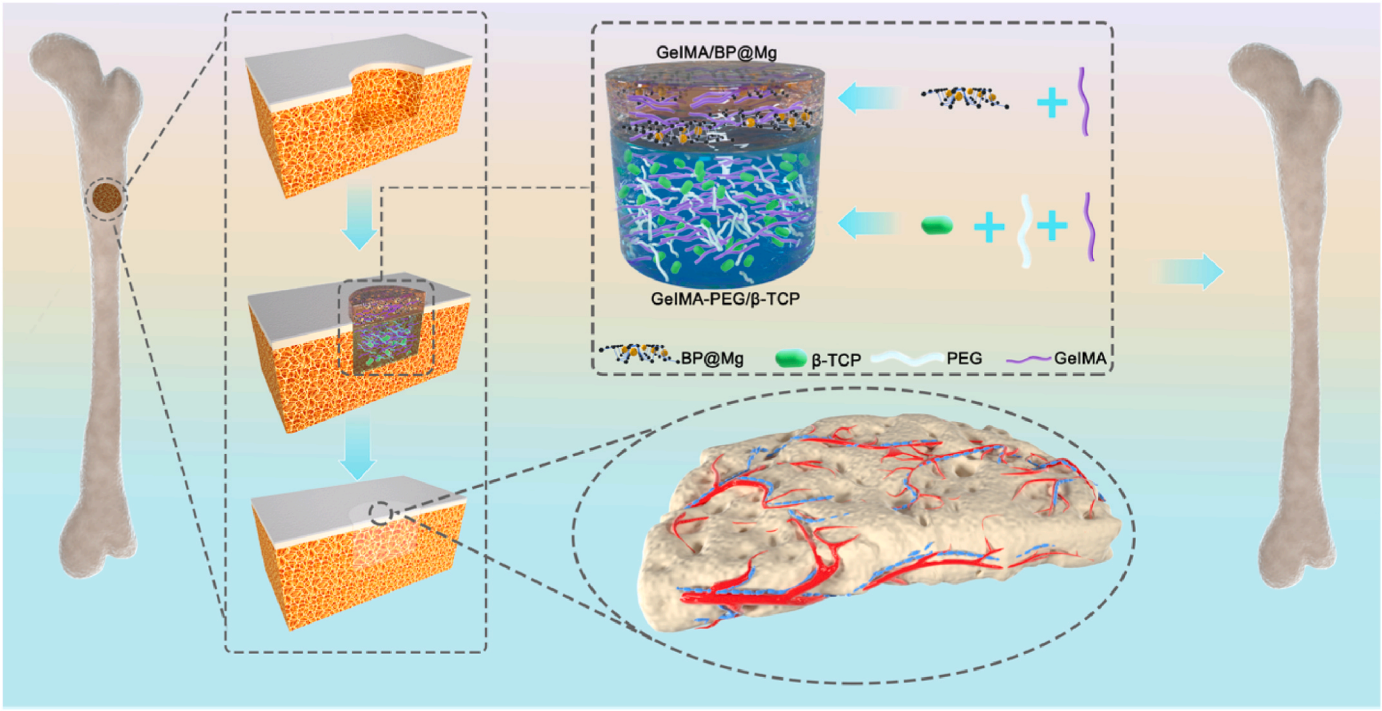

Fig. 1. A schematic diagram of the bilayer hydrogel scaffold for vascularization, neurogenesis, and bone regeneration. The upper (GelMA-BP@Mg) hydrogel served as a periosteal repair layer, while the bottom layer (GelMA-PEG/β-TCP) hydrogel served as a bone repair layer. Together, they accelerated the formation of a periosteal nerve-vascular network that enhanced bone regeneration.

The sensory nerve, for instance, monitors bone density and metabolic activity to regulate bone homeostasis. This process utilizes osteoblast-secreted prostaglandin E2 (PGE2) to activate the PGE2 receptor 4 in sensory nerves, which, in turn, modulates bone formation via inhibition of the central nervous system-mediated sympathetic activity [2]. Moreover, the calcitonin gene-related peptide (CGRP), secreted from both peripheral and spinal cord terminals of the nociceptive neurons, is a direct inhibitor of osteoclast function. Hence, loss of periosteal sensory nerve at the site of bone defect negatively affects fracture-healing [3,4]. Therefore, the rebuilding of periosteal superficial nerves and blood vessels is of great importance to osteogenesis of large segmental bone defects. As such, designing innovative stratified biomimetic constructs, capable of inducing neurovascular regeneration and osteogenesis is highly beneficial in accelerating bone regeneration.

In our previous study, we demonstrated that black phosphorus-incorporated hydrogel strongly promotes neural differentiation [5]. Black phosphorus (BP) nanomaterials, a new member of the two-dimensional (2D) material family, sparks substantial interest among scientists owing to its special physicochemical property, such as, direct band gap, excellent electrical conduction, and good biodegradability. Recently, BP was shown to possess some promising biomedical applications, such as, bone regeneration, drug delivery, and photothermal therapy [6,7]. The BP degradation products are phosphate anions, which are part of bone tissue and contribute to mineralization and accelerate bone repair. There were also researches on the application of BP nano-scaffolds in nerve regeneration. For example, Qian et al. [8] demonstrated that black phosphorus nanoscaffold induced angiogenesis and neurogenesis. But BP has limited ability to promote nerve regeneration. In addition, BP was shown to be very reactive to oxygen and water, owing to the lone electron pair in each phosphorus atom within the puckered layer [9]. This, unfortunately, limits its applications in biomedicine. Recently, it was reported that metal ions modification can greatly improve stability of black phosphorus [10,11]. Moreover, magnesium induces angiogenesis and peripheral nerve repair [12–14]. Given these evidences, we speculated that the introduction of Mg bonding to BP nanosheet surface will markedly augment its stability and biological activity.

To this end, we constructed a bilayer hydrogel scaffold, capable of inducing neurovascular regeneration and osteogenesis simultaneously, that simulated the periosteal structure and enhanced bone regeneration (Fig. 1). The bilayer hydrogel synthesis involved two steps. First, BP nanosheets robustly captured Mg^{2+} via coordination and electrostatic attraction. Second, the bottom GelMA-PEG/β-TCP hydrogel and the upper layer GelMA/BP@Mg hydrogel were synthesized by photocrosslinking GelMA molecules under photoinitiator and ultraviolet. Our results demonstrated that the upper hydrogel layer simulated a bionic periosteal structure, and significantly promoted angiogenesis via induction of endothelial cell migration and simultaneous upregulation of nerve-related protein expression in neural stem cells (NSCs). Moreover, the bottom layer of the hydrogel significantly promoted bone marrow mesenchymal stem cells (BMSCs) activity and osteogenic differentiation. We also employed this bilayer hydrogel structure to correct rat skull defects. Based on our radiological and histological examinations, the bilayer hydrogel scaffolds markedly enhanced early vascularization and neurogenesis, which prompted eventual bone regeneration and remodeling. Our current strategy paves way for designing nerve-vascular network biomaterials for bone regeneration.

2. Materials and methods

2.1. Preparations of BP and BP@Mg nanosheets

Bulk BP crystals synthesis was conducted under elevated temperature and pressure using a cubic press with six tungsten carbide anvils. The red phosphorus lump (Alfa Aesar, 99.999+%) precursor was pressurized at 2 GPa at room temperature (RT) before rapidly heating to a temperature of 1000 °C, followed by a 10 min hold. The bulk BP crystals formed after quenching to RT and subsequent pressure release.

The black phosphorus nanosheets were synthesized via electrochemical exfoliation of corresponding bulk sample. Delamination was

done with a two-electrode systems submerged in propylene carbonate (PC) with tetrabutylammonium hexafluorophosphate (TBA·PF6; 0.01 m), whereby BP crystal served as the cathode and a platinum sheet served as the anode. Delamination initiation was done with a constant potential of −5.0 V. Following this step, we instantly collected the exfoliated BP sheets and electrolyte into a centrifuge tube for additional exfoliation and dispersion of BP sheets into anhydrous acetone via a 1 h sonication process. We next collected the unexfoliated or thick-layered BP sheets via centrifugation at 1500 rpm for 10 min, whereas the BP nanosheets were removed from the electrolyte via an additional centrifugation at 5000 rpm for 10 min. The resulting BP nanosheets were then decanted to prepare for magnesium incorporation.

We introduced 7.5 mg of magnesium acetate to 5 mL BP nanosheets suspension (0.5 mg/mL BP) before probe sonicating for 3 min. Following a 3 h stir, the mixture underwent centrifugation at 5,000 rpm for 15 min. The pellet (BP@Mg) was retrieved and rinsed in deionized water.

2.2. Characterizing BP and BP@Mg

Scaffold characterization was done with a high-resolution transmission electron microscopy (HR-TEM) on a Talos F200X (FEI, The Netherlands) microscope with 200 kV voltage. Raman spectra were measured using the Via Raman Microscope equipment (LabRAM HR800 Horiba, JobinYvon, France) with 532 nm laser excitation. X-ray photoelectron spectroscopy employed a Thermo Fisher Escalab 250Xi system with the Al Kα X-ray source.

2.3. Preparing GelMA-BP@Mg/GelMA-PEG/β-TCP bilayer GeIMA hydrogels

GelMA was acquired from the Aladdin Industrial Corporation (Shanghai, China). Firstly, the GelMA-PEG/β-TCP hydrogel was synthesized via the cross-linking technique. In short, GelMA was mixed in deionized (DI) water at 50 °C for 10 min, before β-TCP (100 mg mL−1), PEGDA, and photoinitiator Irgacure addition, with magnetic stirring. The preparation was adjusted to a final GelMA-PEG/β-TCP hydrogel concentration of 10% (w/v) GelMA, 10% (v/v) PEGDA, 1% (w/v) β-TCP, and 0.05% (w/v) photoinitiator Irgacure 2959. The prepolymer solution was gelatinized under UV light (10 mW cm-2, 365 nm) for 5 min. Next, the GelMA-BP@Mg hydrogel was synthesized, as reported previously [5]. In short, BP@Mg (5 mg mL-1) was introduced to the aforementioned GelMA solution, with magnetic stirring. The final concentration of BP@Mg was maintained at 0.3 mg mL-1. The prepolymer solution was then gelatinized under UV light (10 mW cm-2, 365 nm) for 5 min.

2.4. Characterizing GelMA-BP@Mg/GelMA-PEG/β-TCP bilayer GeIMA hydrogels

Hydrogels were initially rinsed in DI water and lyopholyzed. Next, the dried hydrogel samples were sputter-coated in gold (2 nm thickness, IBS/TM200S, VCR Group, Inc.), before visualization with SEM (Nova NanoSEM 450, FEI, The Netherlands).

A rheometer (Kinexus, Malvern) was employed for all rheological examinations at RT. We added hydrogels (1 cm in diameter and 5 mm in thickness) to the parallel plate. We applied a strain amplitude of 0.5% to maintain linear viscoelastic hydrogel networks during measurements. We assessed hydrogel swelling property with the equilibrium swelling ratio (SR). In short, we weighed (Wd) dried hydrogel disks before immersion in phosphatic buffer solution (PBS) at 37 °C for 24 h. Subsequently, the samples were removed, pat-dried with filter paper, and weighed again (Ws). Finally, SR was calculated as follows: SR = (Ws-Wd)/Wd × 100%.

To evaluate the degradation rate of the hydrogel, hydrogel was immersed in collagenase type II solutions and on an orbital shaker at 100 rpm and 37 ^{o}C. At different time points, the hydrogel samples were taken out and their dry weight was measured to evaluate the degradation rate of the hydrogel.

2.5. Cell culture

We extracted BMSCs from the bone marrow of 3–4 weeks Sprague-Dawley rats, weighing 80 g. We received ethical approval for all animal protocols from the Teaching and Research of Huazhong University of Science and Technology. In short, rat femoral shafts were exposed and subsequently flushed with culture medium to collect BMSCs. The isolated cells were then grown in α-minimum essential medium (α-MEM) with 10% FBS in a 37 °C incubator with 5% CO_2. Only cells between 2 and 5 passages were used for experimentation.

Human umbilical vein endothelial cells (HUVECs) were obtained from the China Center for Type Culture Collection, Wuhan, China. They were grown in vascular cell basal medium in a 37 °C incubator with 5% CO_2. Culture medium was replaced every 3 days.

Mouse neuroectodermal stem cells NE-4C (NSCs) were obtained from the China Center for Type Culture Collection, Wuhan, China and were grown in α-minimum essential medium (DMEM) with 10% FBS in a 37 °C incubator with 5% CO_2.

PC12 cell were obtained from the China Center for Type Culture Collection, Wuhan, China and were grown in Dulbecco's modification of Eagle's medium Dulbecco (DMEM) with 10% FBS in a 37 °C incubator with 5% CO_2.

2.6. Cell survival on hydrogels

Cell viability was assessed with the CCK8 assay. In short, cells were plated in hydrogels and cultured in proliferation medium for a specified duration before cell survival assessment, as per kit directions. We also confirmed cell viability using Calcein-AM and PI fluorescent staining and subsequent analysis.

2.7. Osteogenesis In vitro

To elucidate the capacity of BMSCs to undergo osteogenesis on hydrogels, we transferred hydrogel disks into a 24-well Transwell plate (pore size: 8 mm, Corning, USA), and grew 3×10^5 BMSCs on the hydrogels scaffolds. Osteogenic activity was detected via Alkaline phosphatase (ALP) assay, an early biomarker of osteogenic activity. We used Alizarin Red Staining (ARS) kit (Cyagen, Guangzhou, China) to measure calcium phosphate deposition, a.k.a. mineralization. Cells were thrice rinsed in distilled water prior to image capture and quantification via the ImageJ Software.

2.8. Tube formation and migration assay In vitro

To evaluate HUVECs angiogenesis on hydrogel scaffolds, we conducted the capillary-like tube formation assay. In short, hydrogel samples were submerged in 10 ml of cell culture medium (HUVEC cell medium) during a 24 h incubation at 37 °C, followed by centrifugation at 15,000 rpm for 10 min. The supernatant was carefully collected and sterilized via a 0.22 μm filter (Millipore) prior to use in subsequent experiments. Matrigel was pipetted onto pre-chilled 24-well plates (200 μL Matrigel per well) prior to a 60 min polymerization at 37 °C. Approximately 2×10^4 HUVECs were plated into the Matrigel coated plates carrying culture medium with hydrogel extracts. Following 3 and 6 h incubation periods, the newly formed tubular structures were imaged, and the tubule length, mesh amount, and node amount were measured and counted. On an average, we based our calculations on 3–4 representative images from each sample. To evaluate the effect of hydrogel scaffolds on cell migration. After HUVECs cells were covered with 6-well plates, the monolayer of HUVECs cells cultured in 6-well plates was scratched with sterile pipette tips of 10 μL to produce linear scratches. Then, the cells were cultured in serum-free medium or hydrogel extracts for 24 h, and then imaged by inverted microscope. To further confirmed

Table 1
PCR primers for genes.

Gene	Primer sequence
GAPDH	Forward primers, GCCTCGTCTCATAGACAAGATGGT.
	Reverse primers, GAAGGCAGCCCTGGTAACC
Runx2	Forward primers, CCTTCCCTCCGAGACCCTAA
	Reverse primers, ATGGCTGCTCCCTTCTGAAC
Col-1	Forward primers, CTGAGATGCTCCCTAGACC
	Reverse primers, CCCTTGTTAAATAGCACCTTC
OCN	Forward primers, GAACAGACAAGTCCCACACAG
	Reverse primers, TCAGCAGAGTGAGCAGAAAGAT
Opn	Forward primers, GAGTTTGGCAGCTCAGAGGA
	Reverse primers, TCTGCTTCTGAGATGGGTCA
vWF	Forward primers, CCGATGCAGCCTTTTCGGA
	Reverse primers, TCCCCAAGATACACGGAGAGG
VEGF	Forward primers, TTCAAGCCATCCTGTGTGCC
	Reverse primers, CACCAACGTACACGCTCCAG
CD31	Forward primers, AACAGTGTTGACATGAAGAGCC
	Reverse primers, TGTAAAACAGCACGTCATCCTT
Nestin	Forward primers, AGCACTCCCATCCCACCTAT
	Reverse primers, GGGTTGTGGCTAAGGAGGTC
Tuj1	Forward primers, TAGACCCCAGCGGCAACTAT
	Reverse primers, GTTCCAGGCTCCAGGTCCACC
GFAP	Forward primers, CGGAGACGTATCACCTCTG.
	Reverse primers, TGGAGGCGTCATTCGAGACAA
MAP2	Forward primers, GCCAGCATCAGAACAAACAG.
	Reverse primers, AAGGTCTTGGGAGGGAAGAAC

the angiogenesis induction properties of GelMA-BP@Mg hydrogel. 2×10^4 HUVECs was cultured on the hydrogels for 24h and 48h, the cell morphology observation by staining with rhodamine labeled phalloidin and DAPI and observed with a fluorescence microscope.

2.9. Neural differentiation of NSCs and the morphology of PC12 on hydrogels

NSCs neural differentiation was performed in complete culture medium without the presence of any neurotrophic factors. Culture medium was refreshed every 2 days and the process lasted for 7 days. Cell analysis was done using both immunofluorescent staining and RT-qPCR. Following the 7 day incubation, NSCs were thrice PBS-rinsed before a 10 min fixation in 4% paraformaldehyde, followed by a 5 min permeabilization in 0.5% Triton X-100. Upon blocking with 1% BSA for 1 h, the cells were exposed overnight (ON) to primary antibodies at 4 °C before subsequent exposure to secondary antibodies for 1 h at RT. NSCs were PBS-rinsed thrice, then stained with DAPI. Finally, cells on the scaffolds were visualized with a laser scanning confocal microscope. The utilized primary antibodies were as follows: mouse anti-Nestin (Santa Cruz Biotechnology, Inc.), mouse anti-Tuj1 (Santa Cruz Biotechnology, Inc.), rabbit anti-GFAP (Santacruz Biotechnology, Inc.), and rabbit anti-MAP2 (Santa Cruz Biotechnology, Inc.) antibodies. The corresponding secondary antibodies were as follows: FITC-conjugated goat anti-mouse IgG (1:100 dilution, Santa Cruz Biotechnology, Inc.) and Cy3-conjugated goat anti-rabbit IgG (1:100 dilution, Santa Cruz Biotechnology, Inc.). To observe the morphology of PC12 on hydrogel. Cells were planted on hydrogels for 3 days at a density of 2×10^4 cells per dish. The nuclei were stained green with DAPI and the cell membrane was stained red with Action for observation under fluorescence microscope.

RNA isolation was done with an RNA extraction kit (Takara Bio Inc., Otsu, Shiga, Japan), followed by cDNA synthesis with a PrimeScript-RT Master Mix reverse transcription kit (Takara Bio Inc., Otsu, Shiga, Japan), following kit directions. The qPCR assay employed SYBR Premix Ex Taq (Takara Bio Inc., Otsu, Shiga, Japan). Primer sequences used in this study (GAPDH, Runx2, Col-1, OCN, Opn, VEGF, vWF, CD31, Nestin, Tuj1, GFAP) are listed in Table 1. GAPDH was used as the endogenous control and was used to normalize target gene expression to determine the relative target gene expression.

2.10. Animal experiment

We assessed the early bone forming ability of hydrogel scaffolds in a rat calvarium defect model (Sprague–Dawley, ten-week-old male). In short, the rat cranial surface was surgically exposed and two bilateral, full-thickness, circular (5 mm), critical-sized bone defects were created with the help of a saline-flushed trephine bur. Subsequently, hydrogel scaffold samples were introduced to each calvarial defect, the subcutaneous tissue was closed and the skin was sutured. Animals were euthanized 6 weeks and 12 weeks after implantation and the calvarium tissues were excised and fixed in 10% buffered neutralized formalin for subsequent evaluation.

2.11. Micro-CT analysis of bone defects

The calvarium tissues were visualized under a micro-CT scanner (SkyScan 1176 X-ray microtomography; Bruker) at a resolution of 18 μm for bone regeneration analysis. Following a three-dimensional reconstruction, we computed the bone mineral density (BMD) and the bone volume fraction (BV/TV) of the defects using CT analysis software.

2.12. Histological and immunohistochemical staining

We also decalcified calvarium tissues using EDTA (PH 7.0) at RT, before embedding in paraffin, and cutting into 5-μm thick slices. Next, we conducted two separate histological examinations and three distinct immunohistochemical evaluations to characterize the bone tissue and new vessel formation. Among the stains used were hematoxylin and eosin (H&E), and Masson's trichrome, which evaluated new bone and collagen formation. Among the immunohistochemical staining used was osteocalcin (OCN) staining, which identified mature osteoblasts and osteocytes in the newly formed bone, as well as CD31 (ab28364, Abcam) and beta tubulin III (Ab18207, Abcam), which quantified vessel formation during bone healing. Image J software was employed for quantification of all stains.

2.13. Statistical analysis

All data are expressed as mean ± standard deviation (SD). Data analyses employed the Statistical Package for the Social Sciences software (SPSS 16.0), whereby the analysis of variance (ANOVA), followed by post hoc Tukey's test, was used for data comparison. $P < 0.05$ (confidence level of 95%) was set as the significance threshold.

3. Result and discussion

3.1. Fabrication and characterization of the bilayer hydrogel scaffold

BP nanosheets were synthesized by exfoliating the bulk BP using electrochemical intercalation in a non-aqueous electrolyte, according to our previous studies [5]. BP nanosheets robustly captured Mg^{2+} via coordination and electrostatic attraction. The BP nanosheets, Mg^{2+} modified BP nanosheets (BP@Mg), and β-TCP nanocrystals morphology were characterized via transmission electron microscope (TEM) (Fig. 2-c). Based on our analyses, the average BP and Mg^{2+} modified BP nanosheets sizes were between 2 and 5 μm, and they possessed a standard multilayer structure, based on edge morphology. β-TCP appeared as a short bar and the size was about 200 nm. Following element mapping of the selected BP@Mg nanosheets (Fig. 2i), the phosphorus (P), oxygen (O), and magnesium (Mg) elements were found to be evenly distributed throughout the entire nanosheets, thus confirming the successful incorporation of Mg^{2+} in the BP nanosheets.

Next, we employed Raman spectra to examine BP and BP@Mg nanosheets. Based on the Raman spectra, both nanosheets displayed three distinct peaks (Fig. 2d), similar to what was previously reported [15]. These results indicated that Mg^{2+} modified BP nanosheets

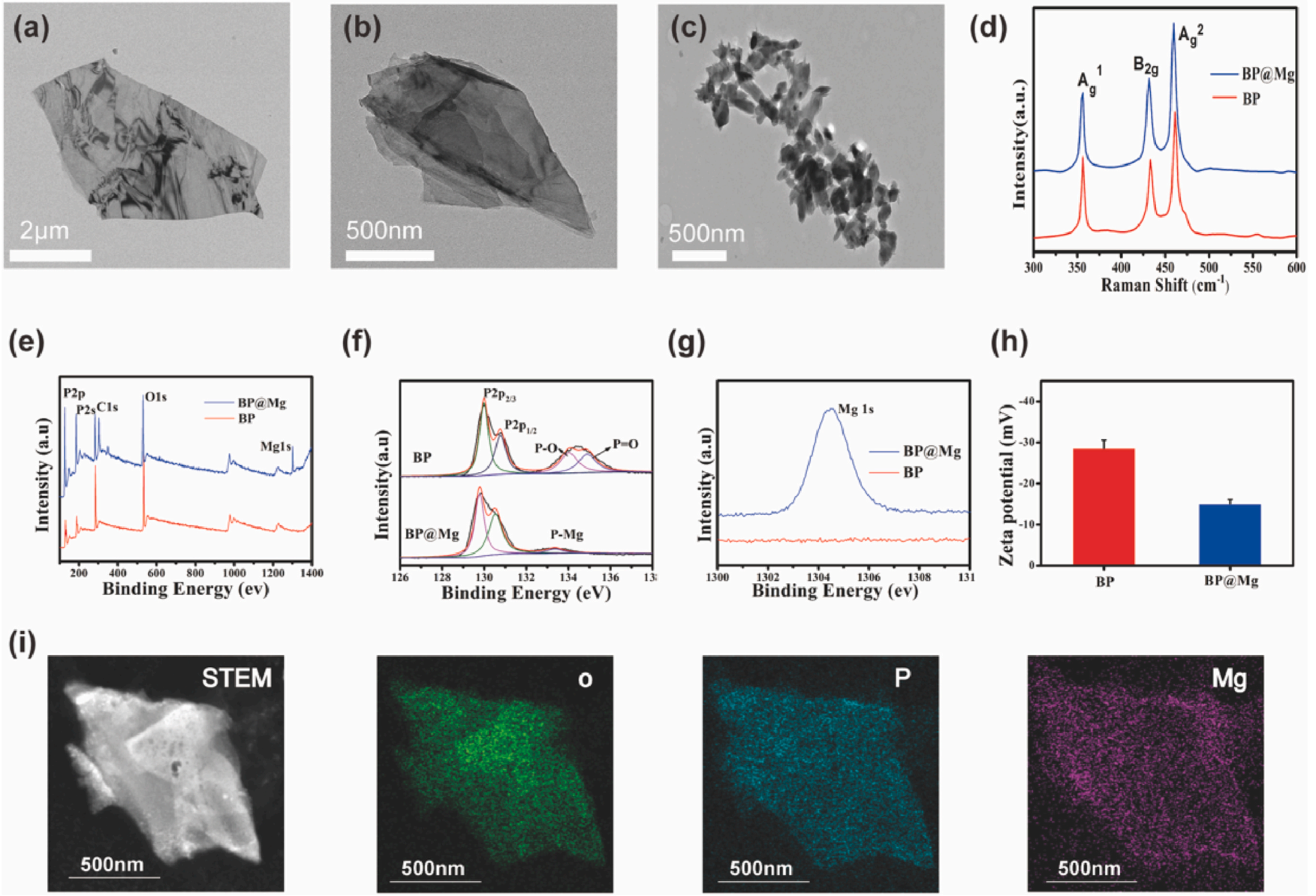

Fig. 2. Characterizing BP and BP@Mg nanosheets. (a) TEM assessment of BP nanosheets. (b) TEM assessment of BP@Mg nanosheets. (c) TEM assessment of β-TCP nanocrystals. (d) Raman spectra of BP and BP@Mg^{2+} nanosheets. (e, f, g) XPS data of BP and BP@Mg nanosheets. (h) Zeta potentials of BP and BP@Mg nanosheets. (i) STEM-EDX elemental mapping of BP@Mg nanosheets.

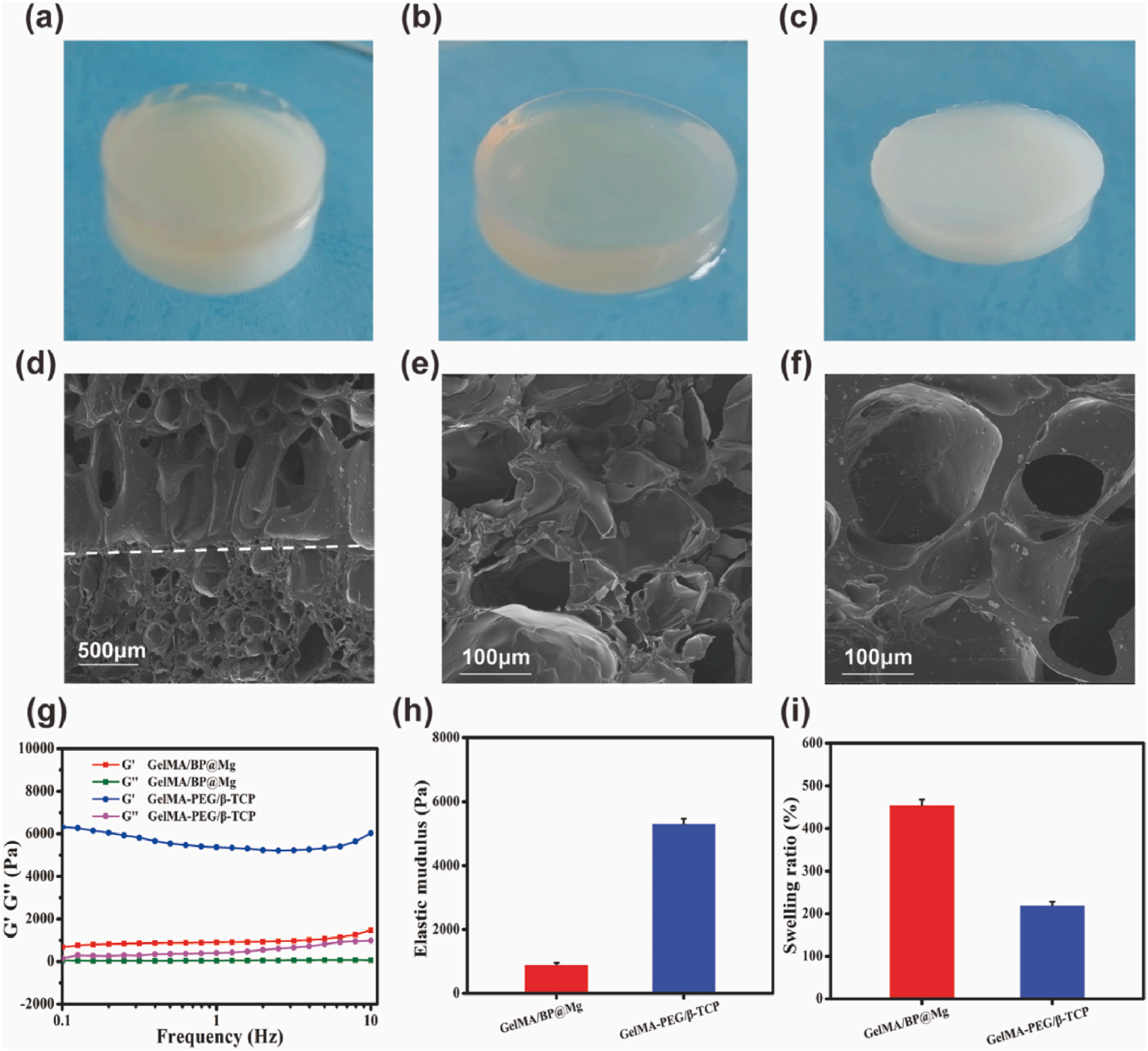

Fig. 3. Characterizing the GelMA–BP@Mg and GelMA-PEG/β-TCP hydrogel scaffolds. Image of (a) bilayer hydrogel, (b) upper hydrogel GelMA-BP@Mg scaffolds, (c) bottom hydrogel GelMA-PEG/β-TCP hydrogel scaffold. SEM image of (d) bilayer hydrogel, (e) GelMA-BP@Mg hydrogel scaffold, and (f) GelMA-PEG/β-TCP hydrogel scaffolds. (g) Storage modulus (G′) and loss modulus (G″) of the GelMA-PEG/β-TCP and GelMA–BP@Mg hydrogel scaffolds. (h) The elastic modulus of the GelMA-PEG/β-TCP and GelMA–BP@Mg hydrogel scaffolds. (i) The swelling ratio of the two types of hydrogels.

preparation did not significantly alter the structure of nanosheets. This was further confirmed by X-ray photoelectron spectroscopy (XPS) (Fig. 2e–g). Based on the BP@Mg nanosheets XPS survey spectrum (Fig. 2e–g), the Mg1s peak appeared at 1305 eV, thus validating the successful incorporation of Mg^{2+} in the BP nanosheets. We next measured the zeta potential (ZP) to assess the effect of Mg modification on the surface charge of BP nanosheets (Fig. 2h). Based on our data, the ZP went from −28.6 mV in unmodified BP nanosheets to −15.1 mV in Mg^{2+}modified BP nanosheets.

The bilayer hydrogel scaffolds (Fig. 3a) were fabricated via a two-step procedure. The upper layer of the GelMA/BP@Mg hydrogel was formed by incorporating BP@Mg into the GelMA matrix (Fig. 3b). The bottom layer of the GelMA-PEG/β-TCP hydrogel scaffold was formed via incorporation of the β-TCP nanocrystals into the double-network hydrogel system, which consisted of two interpenetrating polymer networks composed of GelMA and PEGDA (Fig. 3c). Next, we used scanning electron microscope (SEM) to analyze the pore morphology of the hydrogel scaffold (Fig. 3d–f). GelMA/BP@Mg hydrogel has a larger pore structure than GelMA-PEG/β-TCP hydrogel, and the both types of hydrogels contained a highly porous structure, carrying a pore size of more than100 μm, which facilitated cell growth into the scaffold. The rheological properties of hydrogel were next measured in a certain frequency range (0.1–10Hz) using the frequency scanning method to clarify their viscoelasticity (Fig. 3g and h). Both groups of hydrogels exhibited similar non-linear rheological behavior. The three-dimensional network in the hydrogels system exhibited good stability, likely due to the G′ of each group of hydrogels being greater than G″ in each frequency range [16]. We also observed that GelMA-PEG/β-TCP had a higher elastic modulus than GelMA-BP@Mg, which may be due to the GelMA-PEG/β-TCP hydrogen that was formed by GelMA and PEGDA

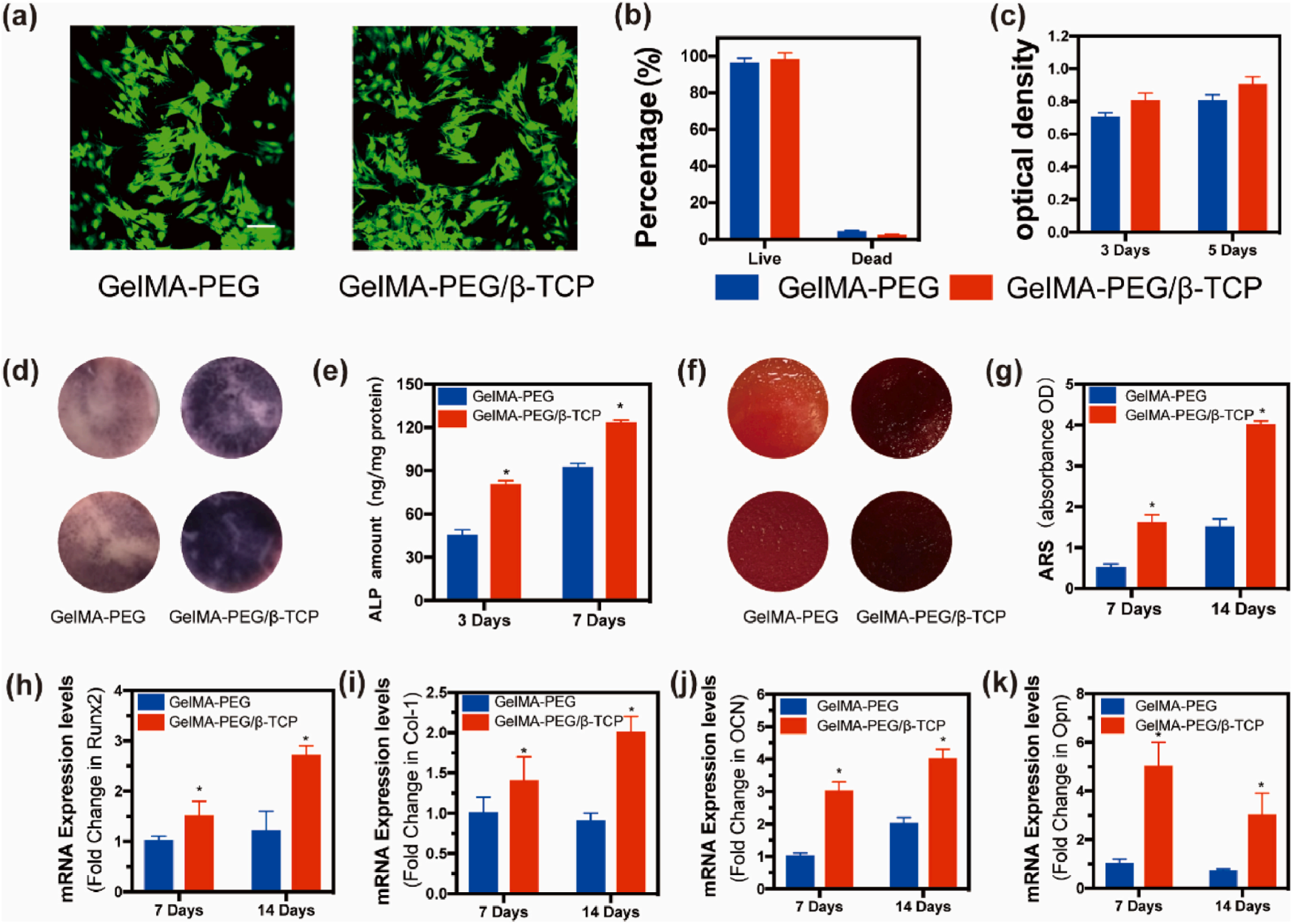

Fig. 4. Cytocompatibility and osteogenic differentiation of GelMA-PEG and GelMA-PEG/β-TCP. (a) Live (green) and dead (red) staining of BMSCs seeded on the GelMA-PEG and GelMA-PEG/β-TCP hydrogel scaffolds. Scale bar = 100 μm. (b) Percentage of live and dead cells on the GelMA-PEG and GelMA-PEG/β-TCP hydrogel scaffolds. (c) BMSC cell survivability on the GelMA-PEG and GelMA-PEG/β-TCP hydrogel scaffolds after 3 and 5 days of culture in proliferation medium. (d) ALP staining and (e) the ALP activity of BMSCs grown on the GelMA-PEG and GelMA-PEG/β-TCP hydrogel scaffolds for 3 days and 7 days. (f) ARS staining of BMSCs cultured on the GelMA-PEG and GelMA-PEG/β-TCP hydrogel scaffolds for 7 days and 14 days. (d) Minerals deposition quantification. (h–k) Relative osteogenic gene expression after 7 and 14 days of BMSCs culture on the GelMA-PEG and GelMA-PEG/β-TCP hydrogel scaffolds. *Represents marked change, relative to GelMA-PEG cells ($p < 0.05$).

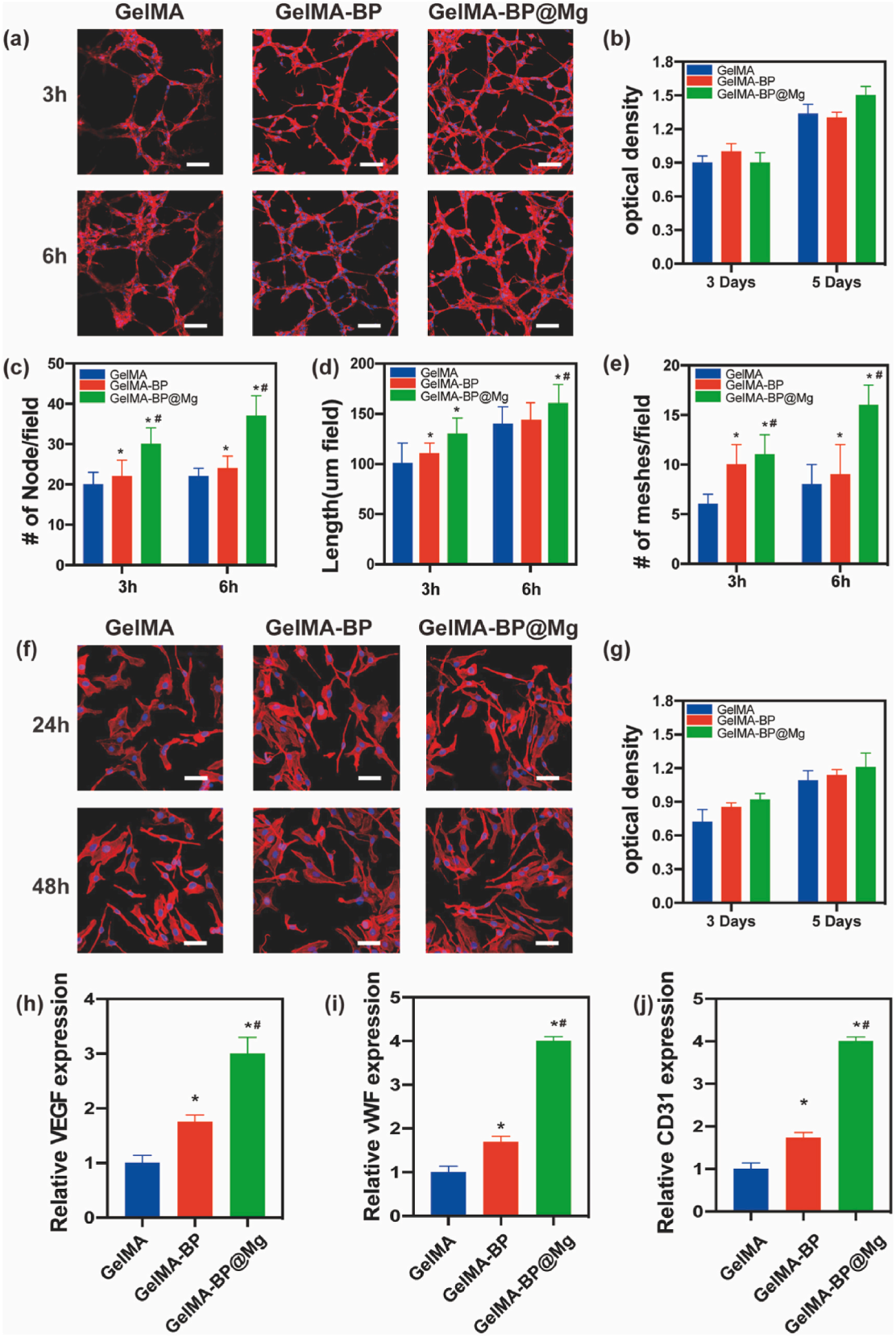

Fig. 5. Angiogenesis assay of HUVECs cultured on hydrogels. (a) Tubule-like structure of HUVECs on Matrigel-coated dish exposed to different hydrogels extracts. Scale bar = 500 μm. (b) Cell viability of HUVECs cultured with the GelMA, GelMA-BP and GelMA-BP@Mg hydrogel extracts. The quantification of angiogenic (c) node number, (d) tubule length and (e) mesh number. (f) Representative images of HUVECs cultured on different hydrogels. Scale bar = 50 μm. (g) Cell viability of HUVECs cultured on different hydrogels. (h–j) Relative angiogenic gene expression after 7 days of culture on the GelMA, GelMA-BP and GelMA-BP@Mg hydrogel. *, # Represents marked change in relation to GelMA and GelMA-BP hydrogel, respectively ($p < 0.05$).

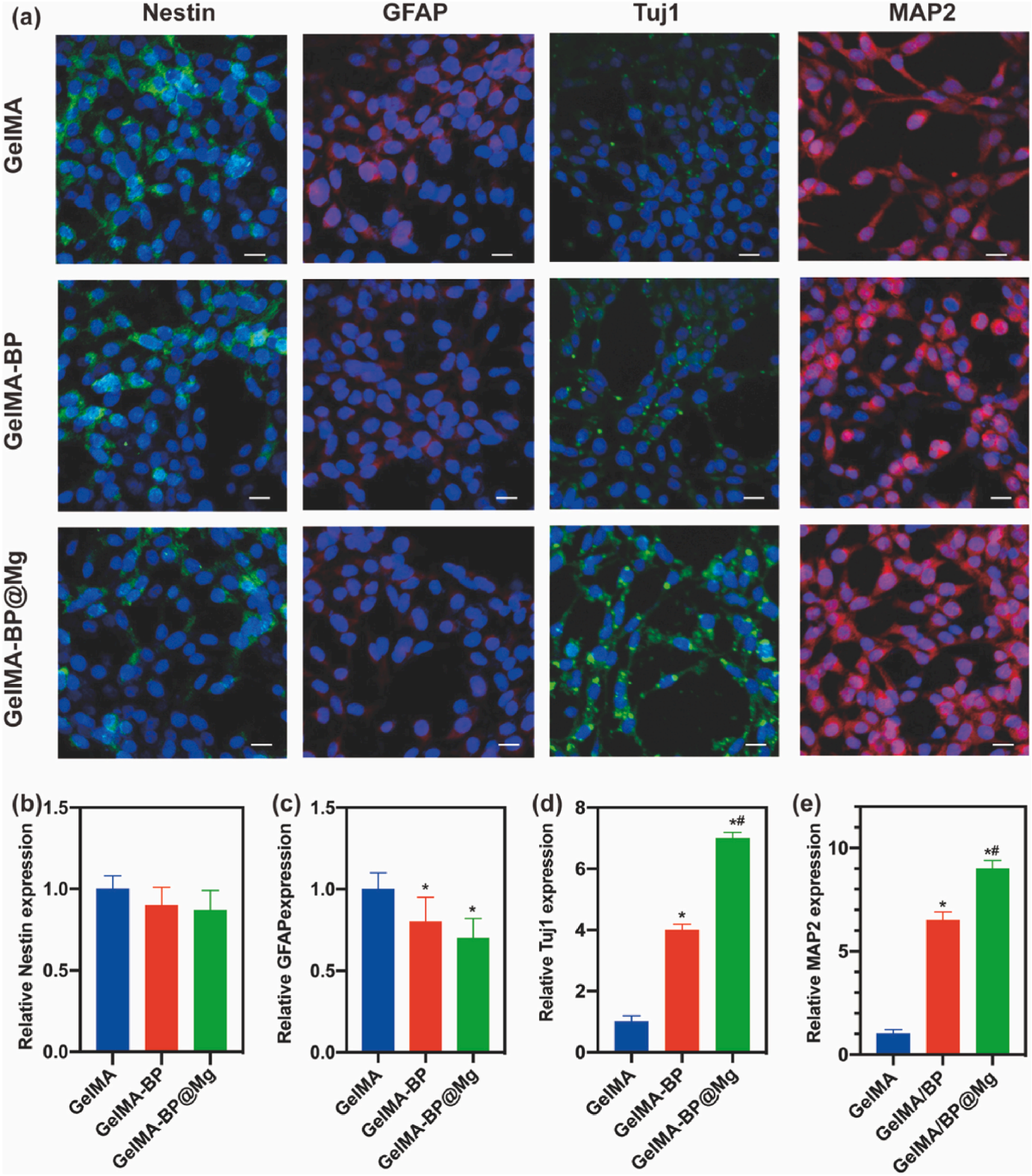

Fig. 6. Stimulation of neural differentiation in cells on the GelMA, GelMA-BP and GelMA-BP@Mg hydrogels. (a) Confocal microscope images of immunostained cells on the GelMA, GelMA-BP and GelMA-BP@PDA hydrogels. Nestin and Tuj1 (green), GFAP and MAP2 (red), and nuclei (DAPI-stained, blue) (scale bar = 20 μm). (b–e) Relative neural-specific gene (Nestin, Tuj1, GFAP, and MAP2) expression in cells on hydrogel scaffolds, as evidenced by RT-qPCR. *, #Represents marked change in relation to the GelMA and GelMA-BP cells, respectively ($p < 0.05$).

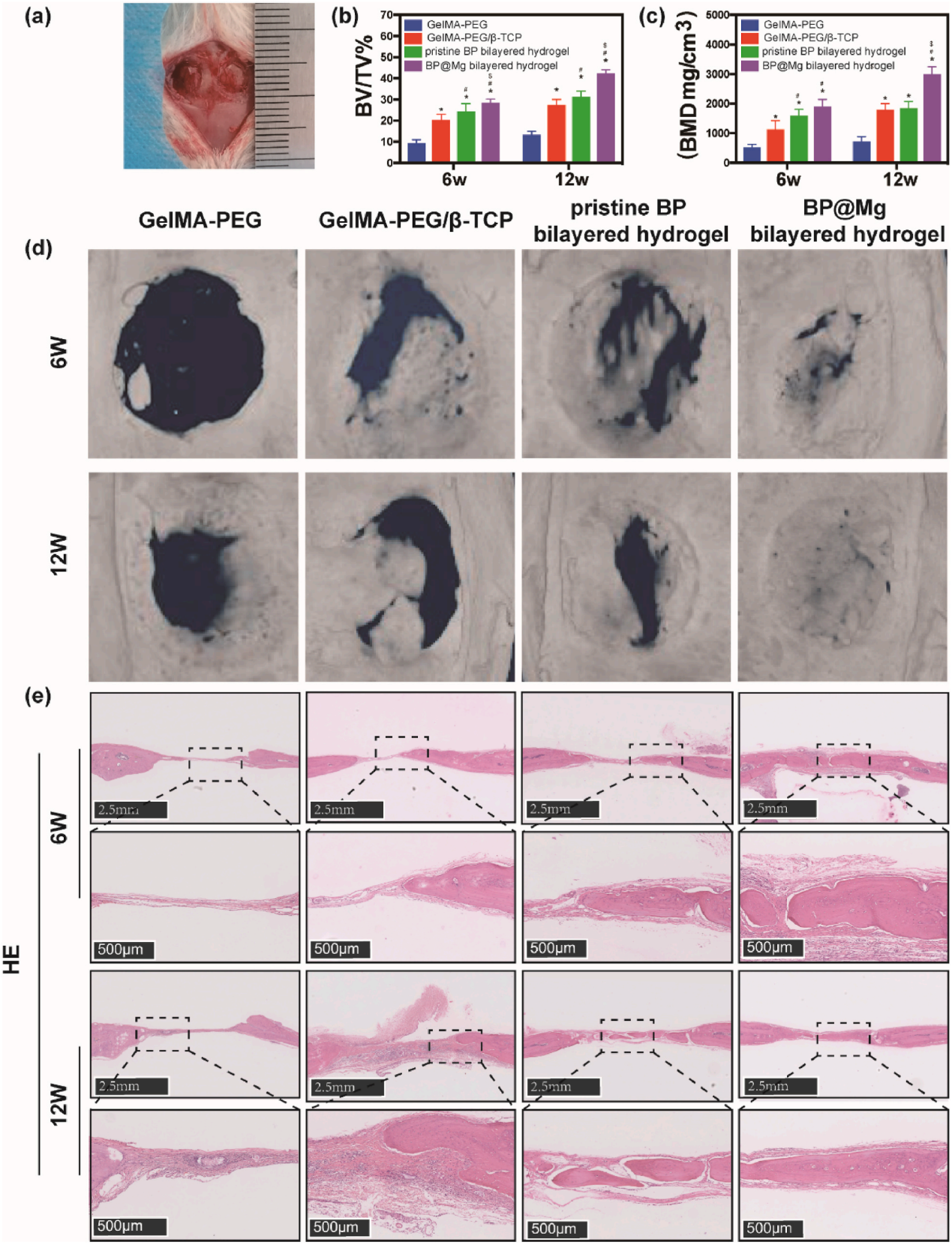

Fig. 7. Bone regeneration of calvarial defects in rats. (a) Calvarial critical-sized defect. (b, c) Micro-CT quantification of the calvarial critical-sized defects. (d) Typical micro-CT images of calvarial defects exposed to four different hydrogel scaffolds. (e) H&E staining. *, #, $ Represents marked change in relation to GelMA-PEG, GelMA-PEG/β-TCP, and pristine BP bilayered hydrogel cells, respectively ($p < 0.05$).

an interpenetrating dual network. In addition, the porous structure suggested that it had good water absorption capacity, which was conducive to supplying proliferating cells with essential nutrients. Typically, water absorption capacity is studied by evaluating the swelling of the hydrogel. As shown in Fig. 3i, GelMA-BP@ Mg hydrogels exhibited higher swelling rates, compared to the GelMA-PEG/β-TCP hydrogels. In vitro biodegradation of the GelMA, GelMA-BP@Mg and GelMA-PEG/β-TCP hydrogel was also investigated. Fig. S1 indicates that the remaining mass of the GelMA-BP@ Mg hydrogels and the GelMA--PEG/β-TCP hydrogels was about 40% and 94% after 72 h in the collagenase type II solutions.

3.2. *In vitro osteogenic, angiogenetic and neurogenesis bioactivities of the biohybrid hydrogel scaffolds*

We, next, examined the biocompatibility of the biohybrid hydrogels. BMSCs were cultured on GelMA-PEG/β-TCP to assess their biocompatibility. The live/dead cells data are summarized in Fig. 4. To enhance our biocompatibility assessment, we stained live cells green with calcein acetoxymethyl ester (Calcein-AM) and dead cells red with propidium iodide (PI). Based on our analysis, only few red-stain dead cells were detected (Fig. 4a). Quantitative analysis of fluorescence images indicated no obvious differences between live cells on the GelMA-PEG versus GelMA-PEG/β-TCP (Fig. 4b), in particular, the amount of live cells was 97.15 ± 0.37% and 98.36 ± 0.51%, respectively. We further confirmed our results with the CCK-8 assay. We demonstrated that the BMSCs on the two hydrogels showed no obvious differences (Fig. 4c). This indicated that the GelMA-PEG/β-TCP hydrogel scaffolds had good biocompatibility. We, next, assessed the early and late markers of osteogenic differentiation, using alkaline phosphatase (ALP) and calcium nodules deposition, respectively. Compared to the GelMA-PEG hydrogel, the staining density of the GelMA-PEG/β-TCP hydrogel was significantly higher. With time, the reaction color became darker (Fig. 4d). Our quantitative results revealed that the GelMA-PEG/β-TCP hydrogel significantly enhanced ALP activity, compared to the GelMA-PEG hydrogel. Moreover, the mineral formation of the GelMA-PEG/β-TCP hydrogel was significantly more, relative to the GelMA-PEG hydrogel at 7 and 14 days of culture/incubation (Fig. 4f and g). In addition, we also evaluated the effect of GelMA-BP@Mg on osteogenic differentiation (Fig. S2). The result showed that the GelMA-BP@Mg can promote osteogenic differentiation, but it is less satisfactory than that of GelMA-PEG/β-TCP. To further validate these data, we assessed the profile of osteogenic differentiation genes, namely, Runx2, CoL-I, Ocn, and Opn, via RT-qPCR. Based on our data, these osteogenic genes were highly expressed in the GelMA-PEG/β-TCP hydrogel at 7 and 14 days, as opposed to the GelMA-PEG hydrogel after the same period of incubation (Fig. 4h–k). In summary, our gene expression results revealed that GelMA-PEG/β-TCP effectively up-regulated expression of osteogenic related genes. β-TCP is known to be both non-toxic and non-irritating, and dissolve easily to release calcium and phosphorus ions, which contributes to neo-bone formation [17–19]. Many researchers combine β-TCP with hydrogel materials with good biocompatibility and bioabsorbability to prepare tissue engineering scaffolds that are more suitable for bone tissue reconstruction [20,21]. In our study, we incorporated β-TCP into the GelMA-PEG double network to prepare the GelMA-PEG/β-TCP hydrogel. Our results suggest that the GelMA--PEG/β-TCP hydrogel possesses great potential to serve as an ideal bioactive scaffold for bone regeneration.

In order to further study the biological properties of the upper-layer hydrogel, the human umbilical vein endothelial cells (HUVECs) and neural stem cells (NSCs) were separately cultured on GelMA-BP@Mg Hydrogel. Hydrogels are ideal materials for tissue engineering scaffolds owing to their biocompatibility, hydrophilicity, and 3D networks that mimic natural tissue [22]. GelMA is denatured collagen, made from chemically modified gelatin, and possess excellent biocompatibility and cell binding moieties that make it an excellent candidate as a base material for tissue engineering [23]. Black phosphorus and magnesium ions are related to blood vessel formation and peripheral nerve repair. Based on our above assessments, we next examined the ability of angiogenesis and innervation of the upper-layer GelMA-BP@Mg hydrogel. First, HUVECs cultured with hydrogel extracts and tested cell viability. The results showed that the GelMA-BP@Mg hydrogel extract had not obvious cytotoxicity (Fig. 5b). Next, we conducted the tubular formation assay to evaluate angiogenesis on scaffolds. HUVECs were cultured with α modified Eagle's medium (α-MEM) containing the leach liquor of GelMA, GelMA-BP, and GelMA-BP@Mg. The HUVECs on the matrix gel formed small tubular structures after 3–6 h of incubation (Fig. 5a) . Calculating node amount, tubule length, and meshes amount clearly revealed that effect of the hydrogel extract (Fig. 5c-e) . Based on our observation, the GelMA-BP@Mg hydrogel extract possessed a significant stimulating effect on various indicators of tubule formation *in vitro*. In addition, the results of migration assay (Fig. S3) showed that the GelMA-BP@Mg hydrogel extract can significantly enhance the migration ability of HUVECs. To further confirmed the angiogenesis induction properties of GelMA-BP@Mg hydrogel. The HUVECs cell was cultured on the different hydrogels, the cell morphology observation showed that HUVECs on GelMA-BP@Mg hydrogel after 24h and 48h cultivation exhibited fiber fusiform shape with most obvious filopodia (Fig. 5f), which meant that the GelMA-BP@Mg hydrogel was beneficial to HUVECs adhesion and growth. The result of CCK-8 indicated that the GelMA-BP@Mg hydrogel had good biocompatibility (Fig. 5g). Next, we also evaluated the gene expression profile of HUVECs cultured on hydrogels for 7 days, particularly, those involved in vessel formation (VEGF, vWF and CD31). We demonstrated an up-regulation of VEGF, vWF and CD31 in the GelMA/BP@Mg hydrogel, relative to the other two hydrogels (Fig. 5h–j). ($p < 0.05$). Magnesium ions are strongly involved in enhancing angiogenesis within the hydrogel scaffold. Collectively, this data indicates that GelMA-BP@Mg plays a positive effect on the angiogenic process.

Aside from osteogenesis and angiogenesis, neurogenesis is also essential for bone formation. Thus, we grew NSCs on the three types of hydrogel scaffolds. Tuj-1 is a critical βIII-tubulin protein that belongs to the microtubule family of proteins. It is involved in intracellular/axonal transport as well as structural maintenance and is considered an early maturing neuronal marker [24]. Nestin is an intermediate filament (IF) protein produced by NSCs and is regarded as a specific marker [25,26]. Nestin levels generally reduce once a differentiated cell forms a neural network [26]. In this study, we immunostained both early (Nestin, Tuj1, and GFAP) and late neural markers (MAP2) to observe differentiated cells (Fig. 6). Based on our analysis, Tuj1 and MAP2 (neural markers) was markedly elevated in the GelMA-BP@Mg scaffold cells, compared to the GelMA and GelMA-BP cells (Fig. 6a). In terms of the glial marker GFAP, GelMA-BP@Mg cells exhibited less GFAP than the other two scaffold cells. To further validate these results, we employed RT-qPCR to examine expression of these genes after NSC neurogenesis for 7 days. Relative to GelMA hydrogels, MAP2 and Tuj-1 levels were significantly increased in GelMA-BP@Mg cells, whereas GFAP levels were slightly decreased in GelMA-BP@Mg cells (Fig. 6b–e). Based on these results, cells on GelMA-BP@Mg hydrogels can substantially enhance neuronal gene expression, compared to the other hydrogels. This indicates that BP modified with magnesium ions can induce the expression of neural markers. In addition, we investigated the effects of GelMA-BP@Mg hydrogels on neurite outgrowth of PC12 cells (Fig. S4), the result showed that GelMA-BP@Mg hydrogels can substantially enhance neurite outgrowth of PC12.

3.3. *In vivo angiogenesis and neurogenesis for bone regeneration of the hydrogel scaffolds*

To further evaluate the repair ability in vivo, GelMA-based bilayer hydrogels were implanted via surgery into the rat calvarial defect model (Fig. 7a) and evaluated after 6 and 12 weeks of implantation. The Micro

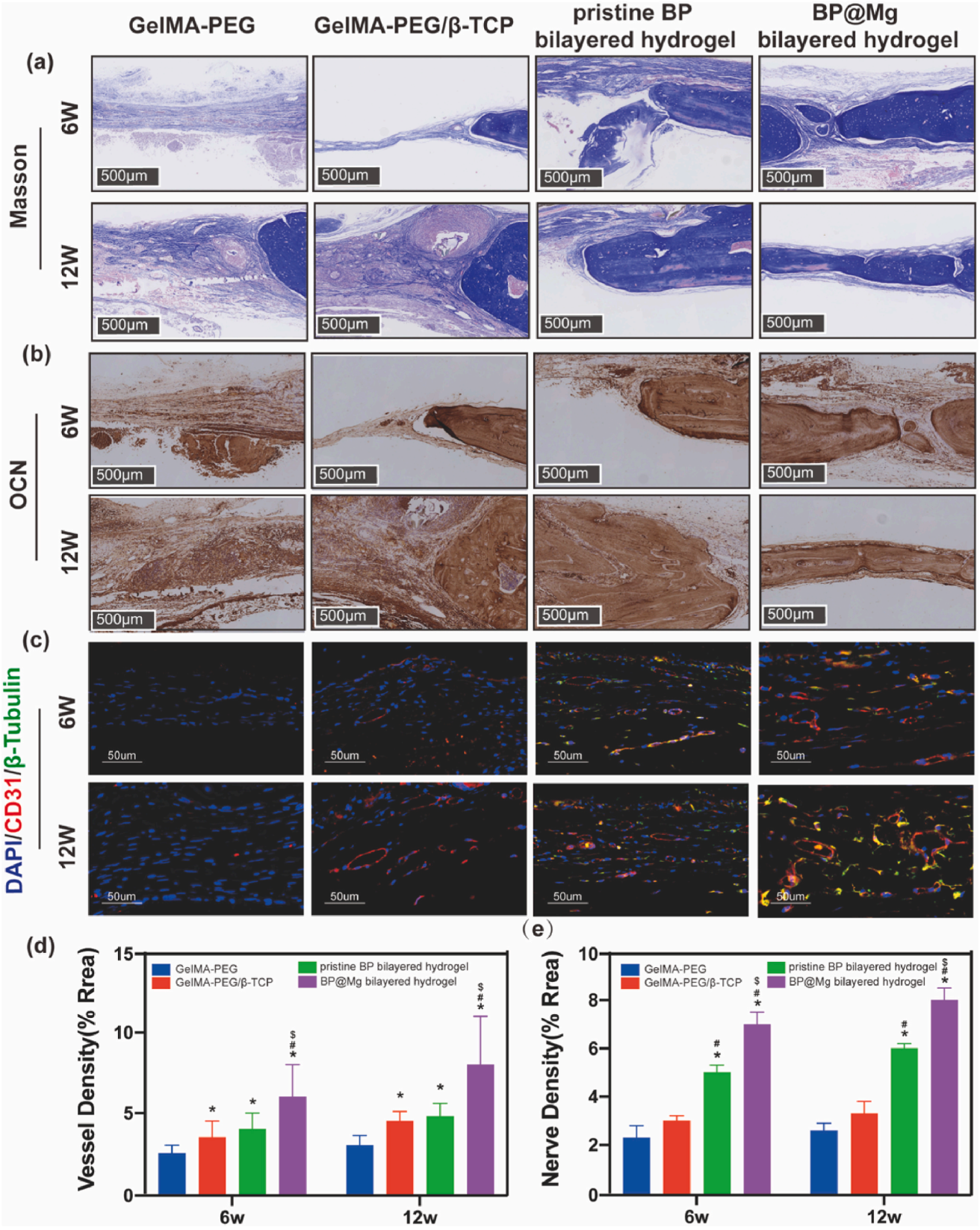

Fig. 8. Bone regeneration and neurovascularization of calvarial defects in rats. (a) Masson staining. (b) OCN-immunohistochemical staining. (c) Typical confocal images of CD31 (blood vessels, red) and β3-tubulin (nerves, green) co-staining on specimen from the calvarial critical-sized defects. (d, e) Blood vessel and nerve density quantification. *, #, $ Represents marked change in relation to GelMA-PEG, GelMA-PEG/β-TCP, and pristine BP bilayered hydrogel cells, respectively ($p < 0.05$).

CT results are presented in Fig. 7b and c. At each time point, the newly formed bone in the BP@Mg cells and pristine BP bilayered hydrogel cells were more obvious than the other two scaffold cells. Moreover, new bone growth started at the defect periphery and moved inward toward the center. At 12 weeks, the rat skull defect in the BP@Mg bilayered hydrogel group was completely covered with newly formed bone. The bone score value (BV/TV%) and bone mineral density (BMD) increased over time, and the BP@Mg bilayered hydrogel group was remarkably higher, relative to the other three at any given time point ($p < 0.05$). Based on the Micro-CT data, the quantified bone regeneration at the defect site from high to low was: BP@Mg bilayered hydrogel > pristine BP bilayered hydrogel > GelMA-PEG/β-TCP hydrogel > GelMA/PEG hydrogel. The results from HE (Fig. 7e), Masson (Fig. 8a), and OCN Masson (Fig. 8b) immunohistochemical staining were also similar to the quantitative micro-CT data. The amount of newly formed bone and collagen tissue in the BP@Mg and pristine BP bilayered hydrogel groups were higher than the GelMA-PEG/β-TCP and GelMA-PEG groups. In terms of the difference between the BP@Mg and pristine BP bilayered hydrogel groups, the addition of magnesium enabled the BP@Mg bilayered hydrogel group to be more effective in bone repair.

CD31 is a marker of neoendothelial cells and is often utilized in angiogenic assessment of implanted materials [27]. β-tubulin III (β3-tubulin) is a neurogenesis-related neuron marker [28]. We immunostained tissue sections with both CD31 (red) and β3-tubulin (green) to qualitatively analyze neovascularization of different hydrogels. We observed positive CD31 and β3-tubulin staining in the bone callus, which suggested successful host vascular infiltration and innervation, respectively. Compared to other groups, the BP@Mg and pristine BP bilayered hydrogel groups markedly enhanced blood vessel and nerve densities at each time point (Fig. 8d and e). Moreover, we detected vessel and nerve co-localization in the BP@Mg and pristine BP bilayered hydrogel groups (Fig. 8c), whereas, no co-localization was observed in the other groups. Comparison between the BP@Mg and pristine BP bilayered hydrogel groups revealed that the BP@Mg bilayered hydrogel group exhibited more effective neovascularization. In addition, to demonstrate the importance of double-layered structures for scaffold systems , the GelMA-PEG/BP@Mg/β-TCP nanocomposite hydrogel was implanted into the rat calvarial defect model , the results of the GelMA-PEG/BP@Mg/β-TCP nanocomposite hydrogel in vivo (Figs. S5 and S6) were not as satisfactory as the BP@Mg bilayer hydrogel, showing that the bilayer system was conducive to improving osteogenic efficiency. Taken together, the BP@Mg bilayered hydrogel promotes neovascularization during osteogenesis , which is conducive to overall healing.

One of the major overlooked factors in tissue engineering is the lack of attention to vascular and nervous networks in bone implants [29]. In most cases, studies developed biomaterials that supported only one tissue (ex. osteoblasts or endothelial cells), while expecting full functionality of the entire bone tissue. However, the nervous system also serves a critical role in bone tissue engineering. In fact, the peripheral nervous system (PNS) actively secretes neuropeptides, which accelerate bone differentiation, activity, and remodeling [30–32]. Multiple other studies also emphasized the role of PNS in bone development and fracture healing [33,34]. Recently, more attention is given to potential BP application in regenerative medicine. Owing to its unique characteristics, BP is used in numerous regenerative medicine researches, including bone, nerve, and blood vessel regeneration. Huang reported that BP hydrogel scaffolds accelerate bone formation by releasing phosphorus ions and captured calcium ions [35]. BP can also oxidize into phosphate to assist nerve regeneration, and ultimately enhance bone regeneration [36]. Angiogenesis and innervation are active coordinated processes present during bone regeneration. Nerve fibers often secrete neuropeptides like substance P (SP) and calcitonin gene-related peptide (calcitonin gene-related peptide, CGRP), which induce angiogenesis [37]. Meanwhile, CGRP and neuropeptide like vasoactive intestinal polypeptide (VIP) promote MSCs proliferation and osteogenic differentiation. Endothelial cells secrete artemisinin and neurotrophic factor 3 (NT-3) to recruit axons, whereas, Schwann cells secrete VEGF to promote angiogenesis. Thus, co-localization of nerves and blood vessels is critical to new tissue generation [38–40]. In this study, we revealed robust neurovascularization and enhanced bone formation in the bilayer GelMA hydrogels cells. Collectively, our data indicate that the BP@Mg bilayered hydrogel efficiently promotes bone healing via support of host neurovascularization capabilities.

4. Conclusion

In summary, we introduced an innovative protocol for neurovascularized bone regeneration. Our structurally and functionally stratified biomimetic hydrogel effectively enhances bone regeneration. The upper layer of hydrogel serves as a bionic periosteum structure, and significantly promotes angiogenesis via accelerating endothelial cell migration meanwhile upregulating nerve-related protein expression in neural stem cells. In addition, the bottom layer of hydrogel significantly promotes BMSC activity and osteogenic differentiation. We also employed this bilayer hydrogel structure to correct defective rat skull. Based on our radiological and histological examinations, the bilayer hydrogel scaffolds markedly enhance early vascularization and neurogenesis, which prompts eventual bone regeneration and remodeling. Our current strategy paves way for designing nerve-vascular network biomaterials for bone regeneration.

Declaration of competing interest

All authors claimed that there was no conflict of interest.

CRediT authorship contribution statement

Yan Xu: Methodology, Validation, Formal analysis, Investigation, Writing – original draft, Writing – review & editing, Visualization. **Chao Xu:** Methodology, Writing – original draft, Writing – review & editing. **Lei He:** Validation, Visualization, Formal analysis, Software. **Junjie Zhou:** Data curation, Resources. **Tianwu Chen:** Visualization, Formal analysis, Software. **Liu Ouyang:** Conceptualization, Investigation. **Xiaodong Guo:** Conceptualization, Methodology. **Yanzhen Qu:** Conceptualization, Methodology, Supervision, Writing – review & editing. **Zhiqiang Luo:** Conceptualization, Methodology, Supervision, Writing – review & editing, Funding acquisition. **Deyu Duan:** Conceptualization, Methodology, Supervision, Writing – review & editing, Funding acquisition.

Declaration of interests

The authors declare that they have no known competing financial interests or personal relationships that could have appeared to influence the work reported in this paper.

Acknowledgment

This study was supported by the National Key Research and Development Program of China (2017YFC1103800).

Appendix A. Supplementary data

Supplementary data to this article can be found online at https://doi.org/10.1016/j.bioactmat.2022.02.024.

References

[1] D. Lopes, C. Martins-Cruz, M.B. Oliveira, et al., Bone physiology as inspiration for tissue regenerative therapies[J], Biomaterials 185 (2018) 240–275.
[2] H. Chen, B. Hu, X. Lv, et al., Prostaglandin E2 mediates sensory nerve regulation of bone homeostasis[J], Nat. Commun. 10 (1) (2019) 181.

[3] C. Adam, A. Llorens, B. Baroukh, et al., Effects of capsaicin-induced sensory denervation on osteoclastic resorption in adult rats[J], Exp. Physiol. 85 (1) (2000) 62–66.
[4] P.J. Apel, D. Crane, C.N. Northam, et al., Effect of selective sensory denervation on fracture-healing: an experimental study of rats[J], J. Bone Joint Surg. Am. 91 (12) (2009) 2886–2895.
[5] C. Xu, Y. Xu, M. Yang, et al., Black-phosphorus-incorporated hydrogel as a conductive and biodegradable platform for enhancement of the neural differentiation of mesenchymal stem cells[J], Adv. Funct. Mater. 30 (39) (2020).
[6] J.R. Choi, K.W. Yong, J.Y. Choi, et al., Black phosphorus and its biomedical applications[J], Theranostics 8 (4) (2018) 1005–1026.
[7] Y. Qing, R. Li, S. Li, et al., Advanced black phosphorus nanomaterials for bone regeneration[J], Int. J. Nanomed. 15 (2020) 2045–2058.
[8] Y. Qian, W.E. Yuan, Y. Cheng, et al., Concentrically integrative bioassembly of a three-dimensional black phosphorus nanoscaffold for restoring neurogenesis, angiogenesis, and immune homeostasis[J], Nano Lett. 19 (12) (2019) 8990–9001.
[9] Y. Liu, P. Gao, T. Zhang, et al., Azide passivation of black phosphorus nanosheets: covalent functionalization affords ambient stability enhancement[J], Angew Chem. Int. Ed. Engl. 58 (5) (2019) 1479–1483.
[10] J.W. Park, T. Hanawa, J.H. Chung, The relative effects of Ca and Mg ions on MSC osteogenesis in the surface modification of microrough Ti implants[J], Int. J. Nanomed. 14 (2019) 5697–5711.
[11] P.C. Wong, S.M. Song, P.H. Tsai, et al., Relationship between the surface roughness of biodegradable Mg-based bulk metallic glass and the osteogenetic ability of MG63 osteoblast-like cells[J], Materials (Basel) 13 (5) (2020).
[12] Y. Gu, J. Zhang, X. Zhang, et al., Three-dimensional printed Mg-doped β-TCP bone tissue engineering scaffolds: effects of magnesium ion concentration on osteogenesis and angiogenesis in vitro[J], Tissue Eng. Regen. Med. 16 (4) (2019) 415–429.
[13] P. Gao, B. Fan, X. Yu, et al., Biofunctional magnesium coated Ti6Al4V scaffold enhances osteogenesis and angiogenesis in vitro and in vivo for orthopedic application[J], Bioact. Mater. 5 (3) (2020) 680–693.
[14] T.M. Hopkins, K.J. Little, J.J. Vennemeyer, et al., Short and long gap peripheral nerve repair with magnesium metal filaments[J], J. Biomed. Mater. Res. 105 (11) (2017) 3148–3158.
[15] H. Liu, A.T. Neal, Z. Zhu, et al., Phosphorene: an unexplored 2D semiconductor with a high hole mobility[J], ACS Nano 8 (4) (2014) 4033–4041.
[16] B. Ren, X. Chen, S. Du, et al., Injectable polysaccharide hydrogel embedded with hydroxyapatite and calcium carbonate for drug delivery and bone tissue engineering[J], Int. J. Biol. Macromol. 118 (Pt A) (2018) 1257–1266.
[17] Q. Li, T. Wang, G.F. Zhang, et al., A comparative evaluation of the mechanical properties of two calcium phosphate/collagen composite materials and their osteogenic effects on adipose-derived stem cells[J], Stem Cell. Int. 2016 (2016) 6409546.
[18] A. Abalymov, L. Van Der Meeren, M. Saveleva, et al., Cells-Grab-on particles: a novel approach to control cell focal adhesion on hybrid thermally annealed hydrogels[J], ACS Biomater. Sci. Eng. 6 (7) (2020) 3933–3944.
[19] M.F. Schulte, S. Bochenek, M. Brugnoni, et al., Stiffness tomography of ultra-soft nanogels by atomic force microscopy[J], Angew Chem. Int. Ed. Engl. 60 (5) (2021) 2280–2287.
[20] X. Li, Z. Chen, H. Zhang, et al., Aligned scaffolds with biomolecular gradients for regenerative medicine[J], Polymers (Basel) 11 (2) (2019).
[21] W. Hao, C. Jiang, M. Jiang, et al., Osteogenic potency of dedifferentiated fat cells isolated from elderly people with osteoporosis[J], Exp. Ther. Med. 14 (1) (2017) 43–50.
[22] Y. Yang, J. Zhang, Z. Liu, et al., Tissue-integratable and biocompatible photogelation by the imine crosslinking reaction[J], Adv. Mater. 28 (14) (2016) 2724–2730.
[23] M. Nikkhah, N. Eshak, P. Zorlutuna, et al., Directed endothelial cell morphogenesis in micropatterned gelatin methacrylate hydrogels[J], Biomaterials 33 (35) (2012) 9009–9018.
[24] A. Gloster, H. El-Bizri, S.X. Bamji, et al., Early induction of Talpha1 alpha-tubulin transcription in neurons of the developing nervous system[J], J. Comp. Neurol. 405 (1) (1999) 45–60.
[25] S. Suzuki, J. Namiki, S. Shibata, et al., The neural stem/progenitor cell marker nestin is expressed in proliferative endothelial cells, but not in mature vasculature [J], J. Histochem. Cytochem. 58 (8) (2010) 721–730.
[26] M.L. Hendrickson, A.J. Rao, O.N. Demerdash, et al., Expression of nestin by neural cells in the adult rat and human brain[J], PLoS One 6 (4) (2011), e18535.
[27] A. Giatromanolaki, M.I. Koukourakis, D. Theodossiou, et al., Comparative evaluation of angiogenesis assessment with anti-factor-VIII and anti-CD31 immunostaining in non-small cell lung cancer[J], Clin. Cancer Res. 3 (12 Pt 1) (1997) 2485–2492.
[28] Q. Shen, S.K. Goderie, L. Jin, et al., Endothelial cells stimulate self-renewal and expand neurogenesis of neural stem cells[J], Science 304 (5675) (2004) 1338–1340.
[29] B.P. Dos Santos, B. Garbay, M. Fenelon, et al., Development of a cell-free and growth factor-free hydrogel capable of inducing angiogenesis and innervation after subcutaneous implantation[J], Acta Biomater. 99 (2019) 154–167.
[30] C. Chenu, Role of innervation in the control of bone remodeling[J], J. Musculoskelet. Neuronal Interact. 4 (2) (2004) 132–134.
[31] S.G. Grässel, The role of peripheral nerve fibers and their neurotransmitters in cartilage and bone physiology and pathophysiology[J], Arthritis Res. Ther. 16 (6) (2014) 485.
[32] T. Fukuda, S. Takeda, R. Xu, et al., Sema3A regulates bone-mass accrual through sensory innervations[J], Nature 497 (7450) (2013) 490–493.
[33] I. Němec, V. Smrčka, J. Pokorný, The effect of sensory innervation on the inorganic component of bones and teeth; experimental denervation - review[J], Prague Med. Rep. 119 (4) (2018) 137–147.
[34] D. Song, X. Jiang, S. Zhu, et al., Denervation impairs bone regeneration during distraction osteogenesis in rabbit tibia lengthening[J], Acta Orthop. 83 (4) (2012) 406–410.
[35] K. Huang, J. Wu, Z. Gu, Black phosphorus hydrogel scaffolds enhance bone regeneration via a sustained supply of calcium-free phosphorus[J], ACS Appl. Mater. Interfaces 11 (3) (2019) 2908–2916.
[36] L. Cheng, Z. Cai, J. Zhao, et al., Black phosphorus-based 2D materials for bone therapy[J], Bioact. Mater. 5 (4) (2020) 1026–1043.
[37] Y. Wang, M. Gupta, T. Poonawala, et al., Opioids and opioid receptors orchestrate wound repair[J], Transl. Res. 185 (2017) 13–23.
[38] Z. Fang, Q. Yang, W. Xiong, et al., Effect of CGRP-adenoviral vector transduction on the osteoblastic differentiation of rat adipose-derived stem cells[J], PLoS One 8 (8) (2013), e72738.
[39] P. Carmeliet, Blood vessels and nerves: common signals, pathways and diseases[J], Nat. Rev. Genet. 4 (9) (2003) 710–720.
[40] Y. Honma, T. Araki, S. Gianino, et al., Artemin is a vascular-derived neurotropic factor for developing sympathetic neurons[J], Neuron 35 (2) (2002) 267–282.